

# Multimode Squeezed State for Reconfigurable Quantum Networks at Telecommunication Wavelengths

Victor Roman-Rodriguez<sup>1,2,\*</sup>, David Fainsin<sup>1</sup>, Guilherme L.

Zanin<sup>1</sup>, Nicolas Treps<sup>1</sup>, Eleni Diamanti<sup>2</sup>, and Valentina Parigi<sup>1</sup>

<sup>1</sup>*Laboratoire Kastler Brossel, Sorbonne Université, ENS-Université PSL,*

*CNRS, Collège de France, 4 place Jussieu, Paris F-75252, France*

<sup>2</sup>*Sorbonne Université, LIP6, CNRS, 4 place Jussieu, 75005 Paris, France*

(Dated: February 5, 2024)

Continuous variable encoding of quantum information requires the deterministic generation of highly correlated quantum states of light in the form of quantum networks, which, in turn, necessitates the controlled generation of a large number of squeezed modes. In this work, we present an experimental source of multimode squeezed states of light at telecommunication wavelengths. Generation at such wavelengths is especially important as it can enable quantum information processing, communication, and sensing beyond the laboratory scale. We use a single-pass spontaneous parametric down-conversion process in a non-linear waveguide pumped with the second harmonic of a femtosecond laser. Our measurements reveal significant squeezing in more than 21 frequency modes, with a maximum squeezing value exceeding 2.5 dB. We demonstrate multiparty entanglement by measuring the state's covariance matrix. Finally, we show the source reconfigurability by preparing few-node cluster states and measure their nullifier squeezing level. These results pave the way for a scalable implementation of continuous variable quantum information protocols at telecommunication wavelengths, particularly for multiparty, entanglement-based quantum communications. Moreover, the source is compatible with additional pulse-by-pulse multiplexing, which can be utilized to construct the necessary three-dimensional entangled structures for quantum computing protocols.

Continuous variable (CV) encoding of quantum information requires the generation of multimode quantum states of light with tailored spectral, spatial and temporal mode properties [1, 2]. In particular, measurement-based protocols rely on the possibility of deterministically generating large multimode entangled states, where entanglement is established between amplitude and phase quadratures of different light modes [3–7], forming what can be described as quantum networks. This in turn requires the generation of a large number of squeezed modes to begin with.

The use of second-order nonlinear waveguides is currently largely explored to generate these tailored squeezed modes: single-mode over a large bandwidth [8–10] or temporally multiplexed [11]. Waveguides are best suited for compact sources compared to cavity-based structures.

Moreover, particular effort has been devoted to generating squeezed sources at telecommunication wavelengths. Single-mode squeezed state [12, 13], on-chip few-mode squeezed states [14, 15] and micro-comb structures have been shown [16]. At these wavelengths optical communication technologies can be exploited [8], enabling quantum state transmission, and hence quantum communication, through fibers over long distances [17] as well as quantum sensing [18]. In particular, spectral clusters can be directly used for frequency-multiplexed QKD [19] and entangled-based multiparty quantum communi-

cation protocols [20].

Scalable quantum networks, in the form of cluster states, are particularly required for quantum computing. Temporal multiplexing has enabled the generation of the largest CV-cluster states to date [5–7]. A photonic fault-tolerant quantum computer [21] requires three-dimensional structures, along with node-selective non-Gaussian operations. While full versatility in the entanglement structure can be reached via fast electro-optical switching [22], CV encoding also requires the ability to fully match the mode-structure in coherent (homodyne) measurement [4].

In this work we pursue scalability in the near infrared C-Band, by demonstrating a resource that is intrinsically spectrally multimode, in a regime where the full multimode structure is accessed and manipulated to form reconfigurable 2-dimensional CV networks [4]. Moreover such a structure is compatible with node-selective non-Gaussian operations [23], and with temporal multiplexing, as it was recently demonstrated in a single-pass configuration [24], thus allowing for 3-dimensional structures [21, 24].

Here, we not only characterize the multimode spectral structure, but we also independently check entanglement correlations between different individual frequency bands. This is done by measuring the full quadrature covariance matrix and applying a Positive-Partial-Transpose (PPT) criterion. Finally, we show the source reconfigurability by generating quantum networks of different topologies and characterizing their quality via the measurement of the so-called nullifier operators.

In our experiment we work with a type-0 waveguide in the degenerate case. The Hamiltonian describing the

---

\* victor.roman@icfo.eu; Currently with ICFO - Instituto de Ciencias Fotonicas, The Barcelona Institute of Science and Technology, 08860 Castelldefels, Barcelona, Spain

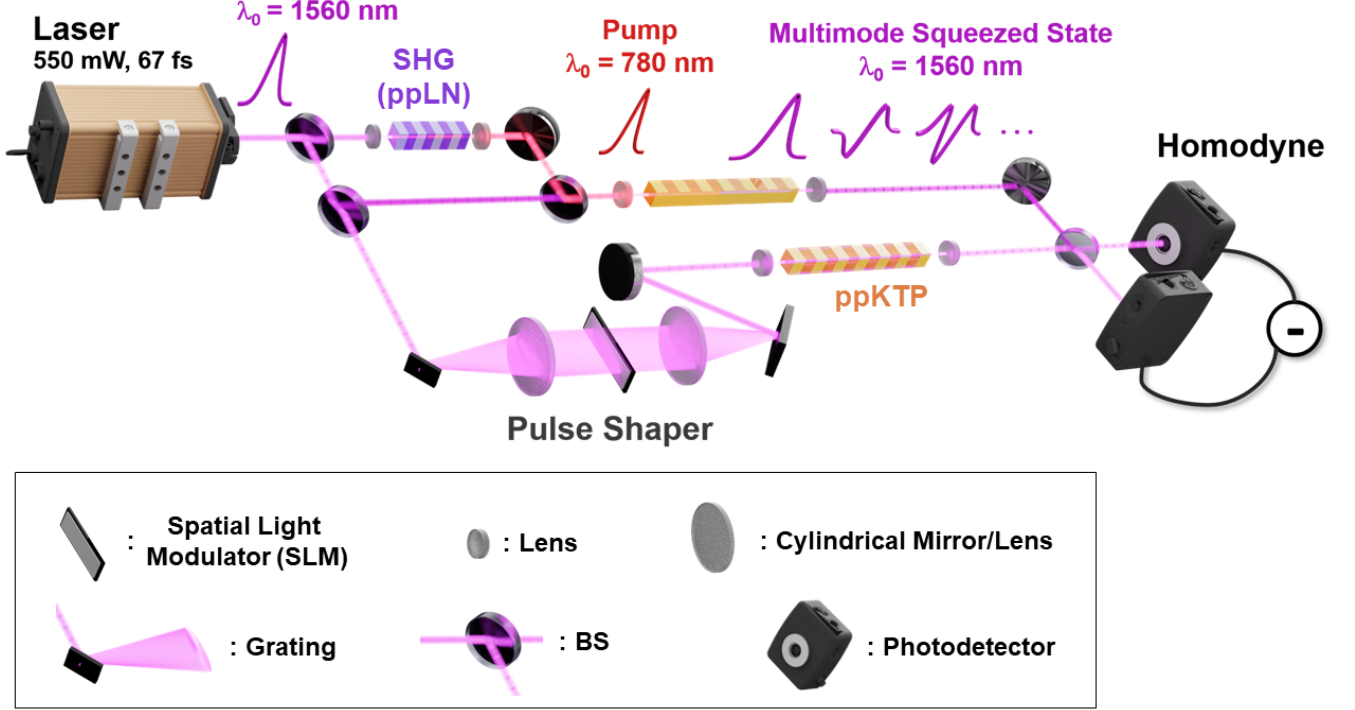


FIG. 1. Experimental scheme for the generation of the multimode states. A telecom wideband pulsed laser is up converted to its second harmonic with a ppLN crystal and then coupled to a nonlinear ppKTP waveguide. Type 0 SPDC interaction generates independent squeezing in a set of frequency modes. Each mode is addressed individually with homodyne detection, where the local oscillator is shaped spectrally with the use of a pulse shaper. For more details see text.

output field of this interaction can be written as [25, 26]:

$$\hat{H} = \sum_{k=1}^N \lambda_k \left( \hat{A}_k^\dagger \right)^2 + \text{h.c.} \quad (1)$$

where  $\{\lambda_k\}$  are called the Schmidt coefficients and the operators  $\{\hat{A}_k\}$  are:

$$\hat{A}_k = \int h_k(\omega) \hat{a}(\omega) d\omega \quad (2)$$

with  $\hat{a}(\omega)$  the annihilation operator of a photon in the plane-wave basis with angular frequency  $\omega$ . The operator  $\hat{A}_k$  is therefore an annihilation operator of photons in the frequency mode  $h_k(\omega)$ .

Evolution under the Hamiltonian of Eq.(1) produces a multimode field with  $N$  independent squeezed states for each of the frequency modes  $\{h_k\}$ , as defined in Eq.(2). Any cluster state with up to  $N$  modes can then be constructed from this multimode field by an appropriate unitary transformation [27, 28]. The specific unitary transformation can be performed by the use of passive optics or equivalently by the projection of the modes in the adequate basis via homodyne detection [1, 4].

The experimental setup for the generation of arbitrary  $N$ -mode cluster states is depicted schematically in Fig. 1.

A broadband fiber femtosecond laser (bandwidth  $\sim 55$  nm, pulse width  $\sim 57$  fs, repetition rate 100 MHz, power  $\sim 550$  mW, centered at 1560 nm), is partly directed to a periodically poled Lithium Niobate (ppLN) crystal, engineered to produce the second harmonic frequency. The ppLN crystal provides light with a bandwidth of  $\sim 2$  nm, centered at 780 nm. This field is then coupled to a single(spatial)-mode, rectangular, nonlinear, periodically poled Potassium Titanyl Phosphate (ppKTP) waveguide [29], which down converts the second harmonic field to the C-band telecom wavelengths and generates multimode squeezed states according to the Hamiltonian in Eq.(1).

On the other side, a large fraction of the original power from the laser is sent to a pulse-shaper in order to generate a spectrally configurable Local Oscillator (LO). The signal field from the waveguide and the LO are mixed and directed to separate photodiodes, whose electrical outputs are subtracted to obtain the homodyne signal.

We implemented the pulse-shaper by diffracting the wavelength components of our input field using a grating, and directing them to a Spatial Light Modulator (SLM), where the light is reflected back and recombined in a similar grating (so called 4f configuration)[30]. In the SLM screen, each pixel, and hence, each frequency component of the field, can be addressed individually, resulting in a

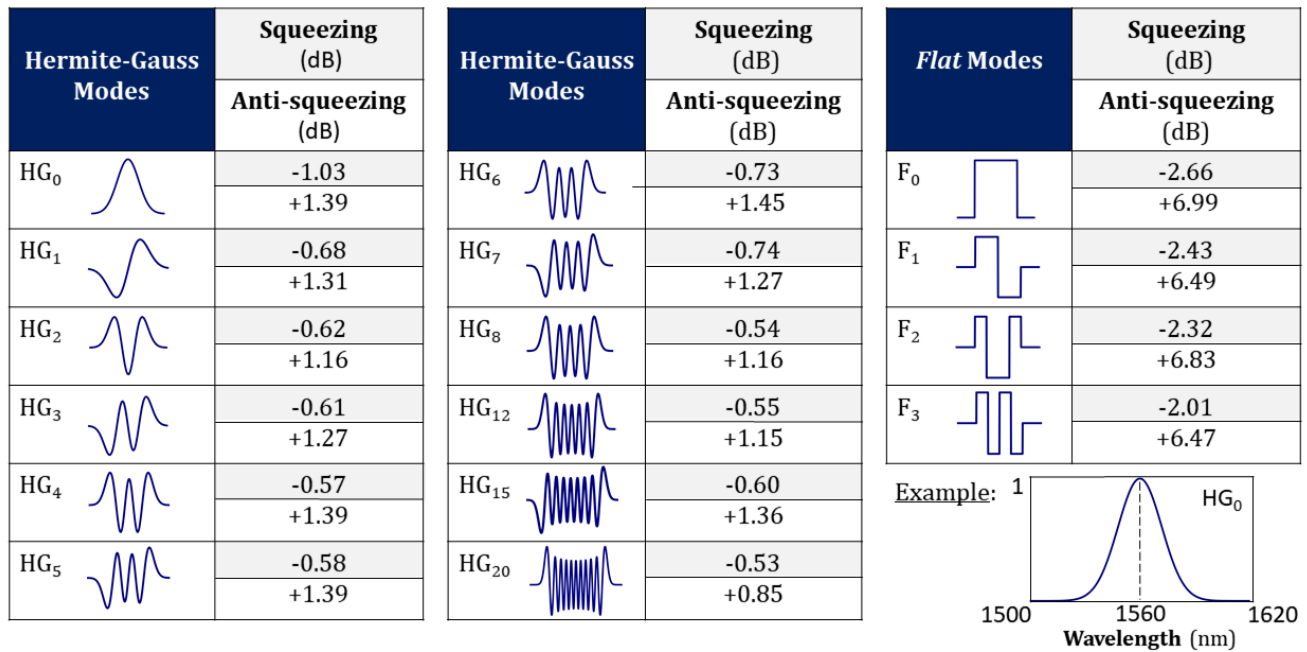


FIG. 2. Experimental squeezing and anti-squeezing values for the Hermite-Gauss modes (left) and the flat modes defined in the text (right). An example of the HG<sub>0</sub> mode is also shown, indicating the spectral range common to all the modes.

spectrally shaped pulse at the output.

The LO is also coupled to another ppKTP waveguide (identical in dimensions) before it mixes with the quantum signal. This is done to spatially match the LO and the signal, effectively decreasing losses in the detection.

We performed numerical simulations to predict the properties of the independent squeezed modes following [26]. Details about these numerical simulations and about the characterization of our waveguides can be found in the Supplemental Material [31].

Fig. 2 summarizes the squeezing values, in dB, obtained in each of the measured modes, where the shot noise stands as reference (0 dB). The signal's quadrature noise was measured with a spectrum analyzer, as a function of the relative phase between the signal and the LO, for different LO spectral shapes. We first projected the output states into the expected family of Hermite-Gauss (HG) modes, where the spectral width of the HG<sub>0</sub> mode in amplitude was 45 nm.

We show in Fig. 2 the measured squeezing and anti-squeezing values of the first 21 HG modes. They are the minimal and maximal values of the quadrature noise measured via averaging on scans of several phase-periods from the spectrum analyzer.

The asymmetry between squeezing and antisqueezing levels is attributed to experimental optical losses, where the main loss source is the non-optimal spatial mode-matching between the signal and LO optical modes. In our case, this can be due to inhomogeneities in the two waveguide structures that are known to appear when the waveguide is long ( $\sim$  cm scale).

We characterize these losses by measuring the visibility of fringes between the LO and a small fraction of telecom light coupled into the waveguides, that resulted to be about 77% in our setup. The associated mode-matching efficiency scales quadratically with the measured visibility.

Another effect in our setup that contributes to equivalent losses is the limitation of the LO bandwidth at the wings of some frequency modes due to the limited physical size of a cylindrical mirror in our pulse shaper. This effect, which is enhanced for higher-order HG modes, is nevertheless not a fundamental limitation of the experiment.

Additionally, we projected the states into a basis of orthogonal and flattened HG modes, that we call *flat* modes. For such modes we observed larger squeezing values - with more than 2 dB of squeezing up to the 4th mode - than for the HG modes. The flat modes and their squeezing levels are shown in the right side of Fig. 2.

Examples of single squeezing traces, possible extra contributions to the global loss sources and details about the flat modes are discussed in the Supplemental Material [31].

This measurement demonstrates the experimental realization of optical multimode squeezed states composed of at least 21 HG frequency modes, as well as larger squeezing values in the set of defined flat modes.

In order to understand better the nature of the correlations in the quantum states, we studied the multimode field in the so-called *frexel* basis, which is composed of 8 equally spaced (about 7 nm) frequency bands covering

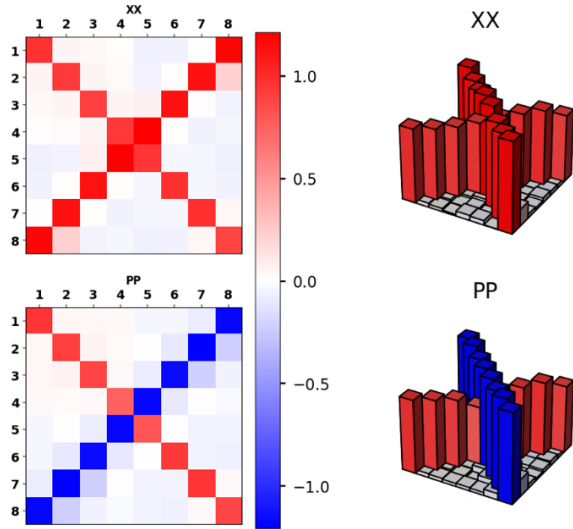


FIG. 3. Expected values of the  $\{\hat{x}_i\hat{x}_j\}$  and  $\{\hat{p}_i\hat{p}_j\}$  quadrature components composing the covariance matrix of the multi-mode state, measured in the frexel basis using 8 frequency bands.

the total spectrum of the LO. Details about the measurement technique used can be found in [32].

We recovered the covariance matrix of the state from the correlation measurement between the frexel quadrature operator components  $\{\hat{x}_i\}$  and  $\{\hat{p}_i\}$ , where  $i$  runs over the number of frexels. The correlation measurements of the type  $\{\hat{x}_i\hat{x}_j\}$ ,  $\{\hat{p}_i\hat{p}_j\}$  are shown in Fig. 3, while correlations of the type  $\{\hat{x}_i\hat{p}_j\}$  are expected to be zero by symmetry arguments [33, 34].

The off-diagonal elements of the covariance matrix indicate the presence of correlations between the frequency bands. In order to test for quantum correlations, i.e. entanglement, we used a positive partial transpose (PPT) criterion [35]. We obtained a violation of the PPT criterion, hence indicating entanglement, for 94% of the possible bipartitions of the state.

A numerical diagonalization of the measured covariance matrix allows us to recover the experimental multi-mode squeezed basis and the squeezing distribution over the modes in this basis (also called *supermodes* [25]). The numerical eigenmodes are in good agreement with the HG modes expected from our theoretical analysis, with a slightly wider spectral width.

Information about the PPT criterion and the diagonalized eigenmodes and eigenvalues can be found in the Supplemental Material [31].

As a note, the frexel basis is of interest, not only because it is easily accessible via the shaping capability of the LO, but also because the frexel modes can be easily spatially separated via dispersive elements and sent to different locations, which is a requisite for potential multiparty quantum communication protocols.

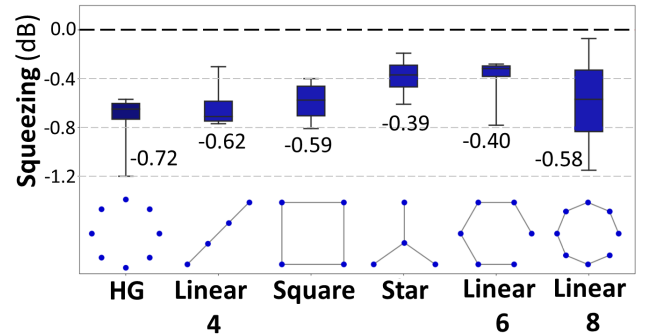


FIG. 4. The boxplots sum up the squeezing value for the first HG modes (left), and the nullifiers of different cluster state size and topologies. The numerical values indicate the mean nullifiers's squeezing value, the black line spread over the squeezing values of the different nullifiers while the blue boxes are related to their variance (they give the amount of values in the interval between the first and third quartiles for each nullifier dataset).

Finally, we used the experimental setup for the deterministic generation of some few-node cluster states, as a proof of principle on the versatility of the source for quantum network generation.

We prove the generation of the cluster states by measuring squeezing in the nullifiers that characterize a specific adjacency matrix, i.e., a particular topology defining the graph. Changing from one topology to another can be achieved by appropriately changing the mask on the pulse shaper [36]. The nullifiers,  $\{\hat{\delta}_i\}$ , of a particular graph with quadratures operators for the nodes denoted  $\hat{x}_i$  and  $\hat{p}_i$  are written as:

$$\hat{\delta}_i = \hat{p}_i - \sum_j V_{ij} \hat{x}_j, \quad (3)$$

where  $V_{ij}$  are the elements of the adjacency matrix defining the cluster state, which is known in advance [27]. Furthermore, the cluster state quality can be qualitatively tested by the amount of squeezing measured in the nullifiers.

We measured 4-node cluster states with different topologies and whose nullifier's level of squeezing is summarized in Fig. 4 via statistical box plots for each cluster topology. Additionally, we show that all nullifiers are squeezed below the shot noise up to the 8-mode linear cluster. The squeezing levels of the nullifiers are smaller than the levels presented in Fig. 2. We suspect this is due to the fact that the used HG modes present some residual correlations, hence affecting the quality of the clusters that are built from that basis. We nevertheless leave further source optimization for future studies and protocol applications. Details about the measurement of the cluster states can be found in the Supplemental Material [31].

In conclusion, we report on a deterministic source of multimode quantum states of light generated via type-

0 SPDC in a nonlinear ppKTP rectangular waveguide. We generated a multimode squeezed vacuum state from which we measured up to 21 squeezed optical spectral modes in the HG basis and over 2 dB of squeezing on four spectral *flat* modes. We measured and diagonalized the covariance matrix in the frexel basis and demonstrated the realization of different cluster states topologies, characterizing them with the squeezing in their nullifier operators.

The quality of the quantum networks can be further en-

hanced by improving the signal-LO mode-matching and the optical configuration of the pulse shaper, both within reach of current technology.

The demonstrated source paves the way towards the implementation of multiparty, entanglement-based quantum communication protocols as well as building scalable resources for quantum computing at telecom wavelengths.

This work was supported by the European Research Council under the Consolidator Grant COQCOoN (Grant No. 820079).

- 
- [1] J. Roslund, R. Medeiros de Araújo, S. Jiang, and N. Fabre, C. Treps, Wavelength-multiplexed quantum networks with ultrafast frequency combs, *Nature Photonics* **8**, 109–112 (2014).
- [2] V. Ansari, J. Donohue, B. Brecht, and C. Silberhorn, Tailoring nonlinear processes for quantum optics with pulsed temporal-mode encodings, *Optica* **5**, 534 (2018).
- [3] M. Chen, N. C. Menicucci, and O. Pfister, Experimental realization of multipartite entanglement of 60 modes of a quantum optical frequency comb, *Phys. Rev. Lett.* **112**, 120505 (2014).
- [4] Y. Cai, J. Roslund, G. Ferrini, F. Arzani, X. Xu, C. Fabre, and N. Treps, Multimode entanglement in reconfigurable graph states using optical frequency combs, *Nat. Commun.* **8**, 15645 (2017).
- [5] S. Yokoyama, R. Ukai, S. C. Armstrong, C. Sornphiphatphong, T. Kaji, S. Suzuki, J.-i. Yoshikawa, H. Yonezawa, N. C. Menicucci, and A. Furusawa, Ultra-large-scale continuous-variable cluster states multiplexed in the time domain, *Nature Photonics* **7**, 982 (2013).
- [6] W. Asavanant, Y. Shiozawa, S. Yokoyama, B. Charoensombutamon, H. Emura, R. N. Alexander, S. Takeda, J.-i. Yoshikawa, N. C. Menicucci, H. Yonezawa, and A. Furusawa, Generation of time-domain-multiplexed two-dimensional cluster state, *Science* **366**, 373 (2019).
- [7] M. V. Larsen, X. Guo, C. R. Breum, J. S. Neergaard-Nielsen, and U. L. Andersen, Deterministic generation of a two-dimensional cluster state, *Science* **366**, 369 (2019).
- [8] A. Inoue, T. Kashiwazaki, T. Yamashima, N. Takanashi, T. Kazama, K. Enbutsu, K. Watanabe, T. Umeki, M. Endo, and A. Furusawa, Toward a multi-core ultrafast optical quantum processor: 43-ghz bandwidth real-time amplitude measurement of 5-db squeezed light using modularized optical parametric amplifier with 5g technology, *Applied Physics Letters* **122**, 104001 (2023), <https://doi.org/10.1063/5.0137641>.
- [9] T. Kashiwazaki, T. Yamashima, K. Enbutsu, T. Kazama, K. Inoue, A. Fukui, M. Endo, T. Umeki, and F. A., Over-8-db squeezed light generation by a broadband waveguide optical parametric amplifier toward fault-tolerant ultrafast quantum computers (2023), arXiv: 2301.12658.
- [10] R. Nehra, R. Sekine, L. Ledezma, Q. Guo, R. M. Gray, A. Roy, and A. Marandi, Few-cycle vacuum squeezing in nanophotonics (2022), arXiv: 2201.06768v.
- [11] H. Tomoda, T. Yoshida, T. Kashiwazaki, T. Umeki, Y. Enomoto, and S. Takeda, Programmable time-multiplexed squeezed light source, *Opt. Express* **31**, 2161 (2023).
- [12] S. Ast, M. Mehmet, and R. Schnabel, High-bandwidth squeezed light at 1550 nm from a compact monolithic ppktp cavity, *Opt. Express* **21**, 13572 (2013).
- [13] T. Gehring, V. Händchen, J. Duhme, F. Furrer, T. Franz, C. Pacher, R. F. Werner, and R. Schnabel, Implementation of continuous-variable quantum key distribution with composable and one-sided-device-independent security against coherent attacks, *Nature Communications* **6**, 8795 (2015).
- [14] F. Mondain, T. Lunghi, A. Zavatta, E. Gouzien, F. Doutre, M. D. Micheli, S. Tanzilli, and V. D’Auria, Chip-based squeezing at a telecom wavelength, *Photon. Res.* **7**, A36 (2019).
- [15] F. Lenzini, J. Janousek, O. Thearle, M. Villa, B. Haylock, S. Kasture, L. Cui, H.-P. Phan, D. V. Dao, H. Yonezawa, P. K. Lam, E. H. Huntington, and M. Lobino, Integrated photonic platform for quantum information with continuous variables, *Science Advances* **4**, 10.1126/sciadv.aat9331 (2018).
- [16] Z. Yang, M. Jahanbozorgi, D. Jeong, S. Sun, O. Pfister, H. Lee, and X. Yi, A squeezed quantum microcomb on a chip, *Nature Communications* **12**, 4781 (2021).
- [17] I. Suleiman, J. A. H. Nielsen, X. Guo, N. Jain, J. Neergaard-Nielsen, T. Gehring, and U. L. Andersen, 40 km fiber transmission of squeezed light measured with a real local oscillator, *Quantum Science and Technology* **7**, 045003 (2022).
- [18] R. Domenegueti, M. Stefszky, H. Herrmann, C. Silberhorn, U. L. Andersen, J. S. Neergaard-Nielsen, and T. Gehring, Fully guided and phase locked ti:ppln waveguide squeezing for applications in quantum sensing, *Opt. Lett.* **48**, 2999 (2023).
- [19] O. Kovalenko, Y.-S. Ra, Y. Cai, V. C. Usenko, C. Fabre, N. Treps, and R. Filip, Frequency-multiplexed entanglement for continuous-variable quantum key distribution, *Photon. Res.* **9**, 2351 (2021).
- [20] G. Murta, F. Grasselli, H. Kampermann, and D. Bruß, Quantum conference key agreement: A review, *Advanced Quantum Technologies* **3**, 2000025 (2020).
- [21] J. E. Bourassa, R. N. Alexander, M. Vasmer, A. Patil, I. Tzitrin, T. Matsuura, D. Su, B. Q. Baragiola, S. Guha, G. Dauphinais, K. K. Sabapathy, N. C. Menicucci, and I. Dhand, Blueprint for a Scalable Photonic Fault-Tolerant Quantum Computer, *Quantum* **5**, 392 (2021).
- [22] L. S. Madsen, F. Laudenbach, M. F. Askarani, F. Rortais, T. Vincent, J. F. F. Bulmer, F. M. Miatto, L. Neuhaus, L. G. Helt, M. J. Collins, A. E. Lita, T. Gerrits, S. W. Nam, V. D. Vaidya, M. Menotti, I. Dhand, Z. Vernon,

- N. Quesada, and J. Lavoie, Quantum computational advantage with a programmable photonic processor, *Nature* **606**, 75 (2022).
- [23] Y.-S. Ra, A. Dufour, M. Walschaers, C. Jacquard, T. Michel, C. Fabre, and N. Treps, Non-Gaussian quantum states of a multimode light field, *Nature Physics* **16**, 144 (2020).
- [24] T. Kouadou, F. Sansavini, A. Matthieu, H. Johan, N. Treps, and V. Parigi, Spectrally shaped and pulse-by-pulse multiplexed multimode squeezed states of light (2022).
- [25] J. Roslund, R. Medeiros de Araújo, S. Jiang, C. Fabre, and N. Treps, Wavelength-multiplexed quantum networks with ultrafast frequency combs, *Nat. Photon.* **8**, 109 (2014).
- [26] V. Roman-Rodriguez, B. Brecht, S. K, C. Silberhorn, N. Treps, E. Diamanti, and V. Parigi, Continuous variable multimode quantum states via symmetric group velocity matching, *New Journal of Physics* **23**, 043012 (2021).
- [27] N. C. Menicucci, S. T. Flammia, and P. van Loock, Graphical calculus for gaussian pure states, *Phys. Rev. A* **83**, 042335 (2011).
- [28] G. Ferrini, J. Roslund, F. Arzani, Y. Cai, C. Fabre, and N. Treps, Optimization of networks for measurement-based quantum computation, *Phys. Rev. A* **91**, 032314 (2015).
- [29] The waveguides were purchased from the company AdvR.
- [30] A. Monmayrant, S. J. Weber, and B. Chatel, A newcomer's guide to ultrashort pulse shaping and characterization, *Journal of Physics B: Atomic, Molecular and Optical Physics* **43**, 103001 (2010).
- [31] See Supplemental Material at (link) for additional measurements and analysis.
- [32] T. Kouadou, F. Sansavini, M. Ansquer, J. Henaff, N. Treps, and V. Parigi, Spectrally shaped and pulse-by-pulse multiplexed multimode squeezed states of light, *APL Photonics* **8**, 086113 (2023).
- [33] G. Patera, N. Treps, C. Fabre, and G. G. J. de Valcárcel, Quantum theory of synchronously pumped type i optical parametric oscillators: characterization of the squeezed supermodes, *Eur. Phys. J. D* **56** (2010).
- [34] F. Arzani, C. Fabre, and N. Treps, Versatile engineering of multimode squeezed states by optimizing the pump spectral profile in spontaneous parametric down-conversion, *Phys. Rev. A* **97**, 033808 (2018).
- [35] R. Simon, Peres-horodecki separability criterion for continuous variable systems, *Phys. Rev. Lett.* **84**, 10.1103/PhysRevLett.84.2726 (2000).
- [36] P. Van Loock, C. Weedbrook, , and M. Gu, Building gaussian cluster states by linear optics, *Phys. Rev. A* **76**, 10.1103/PhysRevA.76.032321 (2007).
- [37] A. B. Fallahkhair, K. S. Li, and T. E. Murphy, Vector finite difference modesolver for anisotropic dielectric waveguides, *J. Lightw. Technol.* **26**, 1423 (2008).
- [38] R. Kumar, E. Barrios, A. J. MacRae, E. C. Cairns, E. H. Huntington, and A. I. Lvovsky, Versatile wideband balanced detector for quantum optical homodyne tomography, *Optics Communications* **285**, 5259 (2012).
- [39] D. K. Serkland, M. Fejer, R. L. Byer, and Y. Yamamoto, Squeezing in a quasi-phase-matched linbo3 waveguide, *Opt. Lett.* **20**, 1068 (1995).
- [40] T. Umeki, O. Tadanaga, A. Takada, and M. Asobe, Phase sensitive degenerate parametric amplification using directly-bonded ppln ridge waveguides, *Opt. Express* **19**, 6326 (2011).
- [41] R. Medeiros de Araújo, J. Roslund, Y. Cai, G. Ferrini, C. Fabre, and N. Treps, Full characterization of a highly multimode entangled state embedded in an optical frequency comb using pulse shaping, *Phys. Rev. A* **89**, 10.1103/PhysRevA.89.053828 (2014).

## Appendix A: Numerical simulation of the multimode state in our experimental configuration

Numerical simulations were performed in order to predict the properties of the independent squeezed modes at the output of the waveguide.

The quantum state after a SPDC interaction is determined by the joint-spectral amplitude (JSA):

$$J(\omega_s, \omega_i) = \sum_k \lambda_k h_k(\omega_s) g_k(\omega_i), \quad (\text{A1})$$

where  $\omega_{s/i}$  is the signal/idler frequency,  $\lambda_k$  are the Schmidt coefficients and  $h_k(\omega_s)$  ( $g_k(\omega_i)$ ) are the signal (idler) frequency modes composing the signal (idler) field after the interaction. In the degenerate case, as it is the case in this work, signal and idler fields are identical and there is a single outfield field after the interaction.

Given the experimental values measured from the second harmonic field (hence the pump to the ppKTP waveguide), and the chosen waveguide dimensions (3 by 3  $\mu\text{m}$  and 15 mm in length), the results of the numerical JSA and its singular value decomposition are shown in Fig. 5. A number of about 34 modes is expected with the Schmidt distribution,  $\{\lambda_k\}$ , shown in the figure. The first three frequency modes, approximating Hermite-Gauss modes, are also shown. For more details about the numerical simulation of the nonlinear waveguides and how the experiment was designed, see [26].

## Appendix B: Waveguide Characterization

The characterization of our waveguides was performed by coupling them to the C-band wavelength (central wavelength: 1560 nm), as well as the second harmonic field (central wavelength: 780 nm). See Fig.8 for a physical photo of the waveguide setup in the lab. A measurement of the spectrum of the second harmonic field produced by the C-band input gives a qualitative estimate on the homogeneity of the waveguide along the propagation direction (a sinc-like function is to be measured, which is the response to a square nonlinear profile by the Fourier transform, expected from a homogeneous non-linear coefficient). The amount of second harmonic produced from the telecom input gives an estimate on the nonlinear coefficient of the waveguide, that is fitted from data in the next section. Finally, a measurement of the spatial profile of the output telecom light (see Fig.9 for some examples of this measurement) can be compared with a numerical simulation (in our case with a finite element method implemented based on [37]) to check the single-spatial-mode feature of the waveguides at telecom wavelengths, and the deviation from the expected fundamental mode propagating in the actual structure.

The homodyne measurement was performed with a home-made detector, including the two photodetectors and the transimpedance circuit outputting the homodyne

electrical signal. The total homodyne efficiency,  $\eta_h$ , can be decomposed in the following terms:

$$\eta_h = \eta_{\text{PD}} \cdot \eta_{\text{el}} \cdot \eta_{\text{opt}} \cdot \eta_{\text{mod}}, \quad (\text{B1})$$

where  $\eta_{\text{PD}}$  is the photodetector's efficiency (around 85% in our case),  $\eta_{\text{opt}}$  is related to the optical losses in the homodyne circuit (near unity in our case),  $\eta_{\text{mod}}$  is the mode matching efficiency, *i.e.*, how close are the LO and the signal in terms of polarization, spatial and temporal profile when interfering, and  $\eta_{\text{el}}$  is the electronic efficiency.

The electronic efficiency can in turn be written as  $\eta_{\text{el}} = 1 - 1/\text{SNR}$  [38], with SNR the signal to noise ratio, *i.e.*, the ratio between the shot noise at a certain input intensity and the value in the absence of any input signal (electronic noise). We measured the best signal-to-noise ratio (also called clearance, if one measures it in dB) at a demodulation frequency of 2 MHz, where the clearance was about 20 dB at 2 mW of input power.

The mode-matching efficiency was limiting the amount of available squeezing in our experiment as it is discussed in the main text. Such term scales quadratically with the visibility between LO and signal and it can be measured by mimicking the signal via an intense beam following the same path as the signal in the experiment, and making it interfere with the LO. The 77% value reported in the main text has been measured with a beam matching the spectral width of the LO. In the case of the measurement of the Hermite-Gauss basis, for higher-order modes we expect a lower mode-matching efficiency, since this spectral matching is poorer.

## Appendix C: Phase Sensitive Amplification Results

Before measuring the multimode squeezing curves shown in the main text, we built a degenerate Optical Parametric Amplifier, or OPA, by pumping the waveguide with a relatively intense seed field at telecom wavelengths (taken directly from the ultrafast laser) and a pump field (from our second harmonic ppLN crystal at 780 nm).

The phenomenon of parametric amplification can be observed as a modulation of the seed amplitude at the output of the waveguide, depending on the relative phase between the seed and the pump fields. This measurement allows us to show the existence of parametric gain in our waveguides, which is a precondition of squeezing generation, even though the levels of multimode squeezing cannot be predicted in this way.

The extrema of the parametric gain,  $G_{\pm}$ , can be approximated, for a single-mode OPA, as [39, 40]:

$$G_{\pm} \sim \exp(\pm 2\sqrt{\eta_{\text{PSA}} P}), \quad (\text{C1})$$

with  $P$  the pump power and  $\eta_{\text{PSA}}$  the parametric efficiency. Ideally, the minimum deamplification,  $G_-$ , should be symmetric with respect to  $G_+$ , although a disparity between the two has been attributed to a distortion of the spatial or temporal profile inside the nonlinear

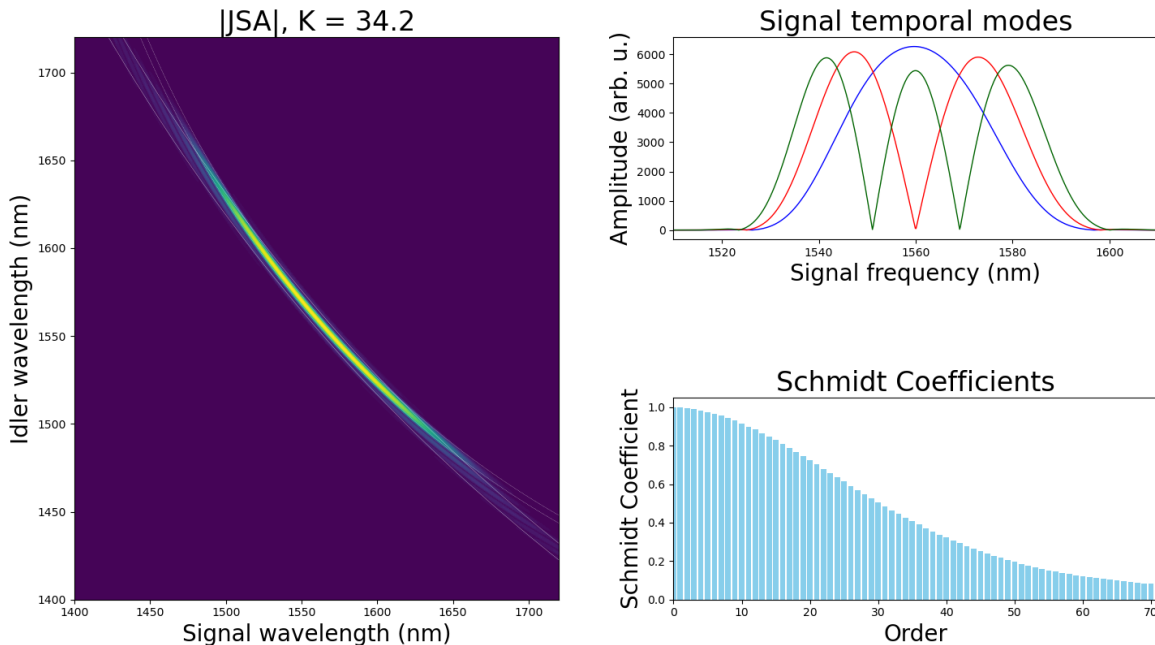


FIG. 5. Numerical simulation of the independent squeezed states. Left: JSA function, Right: First three frequency modes, approximating Hermite-Gauss modes, and the distribution of the Schmidt coefficients.

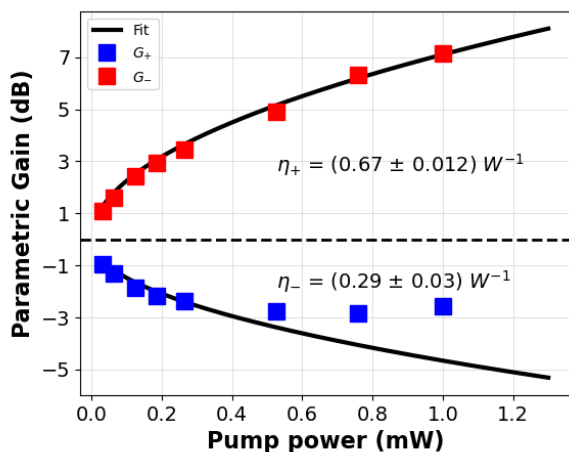


FIG. 6. Parametric gain vs pump power. Extrema in the modulation of the amplitude for the degenerate OPA, fit to Eq. (C1) gives the parametric efficiency, related to the total squeezing level.

material in previous experiments. The disparity appears at sufficiently high power density in the material.

Fig. 6 shows the parametric gain measured as a function of the pump power. The data fits well Eq. (C1) and

gives two values for the parametric efficiency due to their asymmetry. A measurement of the second harmonic efficiency in the same nonlinear waveguide gives an efficiency of  $\eta_{\text{SHG}} = 0.33 \text{ W}^{-1}$ , which is in good agreement with the extracted parametric efficiency for the deamplification.

The conclusion of the phase sensitive experiment is that, at pump powers of few mW, we can expect at least some dB of total squeezing in our multimode states, which are the final measured values showed in the main text.

#### Appendix D: Squeezing curves

The squeezing (antisqueezing) values presented in the main text were obtained by averaging 15 minima (maxima) from the modulated phase signal for each Hermite-Gauss mode, performing homodyne detection with a linear phase shift in time via a piezoelectric mirror. Examples of such traces are depicted in Fig. 7 for the first few modes. The mean squeezing and anti-squeezing values where computed after applying a Savitsky-Golay filter to smooth the data without distorting the signal avoiding unwanted local extrema. The local extrema generated by the piezoelectric mirror when changing direction were intentionally disregarded.

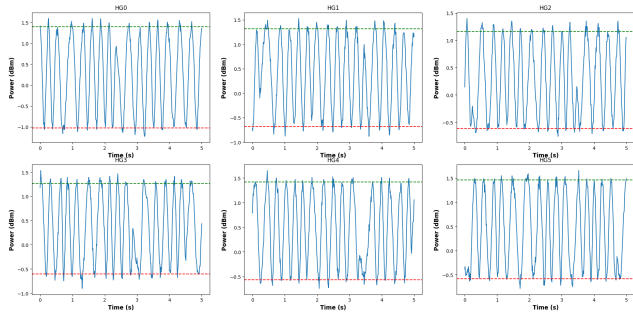


FIG. 7. Squeezing traces for the projection onto the first six Hermite Gauss modes. The average squeezing and anti-squeezing values are shown as the dotted red and green horizontal lines.

### Appendix E: Independent Hermite-Gauss modes

An experimental detrimental effect in the setup described in this work is what we call *optical clipping*, which arises due to the limited size of a cylindrical mirror responsible for focusing the light beam onto the SLM for pulse shaping. Since the beam comes from a refractive element (a grating), some wavelengths at the extremes of the spectrum are cut off. Due to this effect, the LO spectral extremes cannot be used in homodyne detection (the corresponding clipped regions from the different modes are shown in red in Fig. 11). We would then expect even larger values for the measured squeezing levels if the full spectrum was experimentally available.

As a consequence of optical clipping, the 21 Hermite-Gauss modes implemented in the experiment were not exactly orthogonal, with the effect being more pronounced the larger the mode order. Therefore, the actual number of measured modes is expected to be lower than 21. This number depends on the dimensionality of the vector space spanned by the non-orthogonal modes. In order to account for that, we evaluate the rank of the matrix composed by these modes performing a singular value decomposition on the set of 21 vectors after measuring the non-available interval of wavelengths and subtracting it from the HG spectrum. The non-zero singular values count the number of linearly independent modes and hence the dimension of the space we are looking for. The singular values resulting from the decomposition is summarized in Table I.

Since this is a numerical computation, we need a somewhat arbitrary criterion to give a whole number indicating the dimension of our vector space from this result. In our case, we obtain the dimension of the vector space by accounting for singular values that are at least 10% of the highest one. This criterion gives us 18 linearly independent modes. The value being close to the 21 Hermite-Gauss modes indicates that the optical clipping did not have a large impact in reducing the dimensionality of the modes measured in the experiment.

Although the optical clipping is not a fundamental lim-

Mode Number	Singular Value
0	1.42
1	1.40
2	1.31
3	1.28
4	1.21
5	1.19
6	1.18
7	1.12
8	1.09
9	1.08
10	1.02
11	0.99
12	0.97
13	0.94
14	0.90
15	0.84
16	0.60
17	0.30
18	0.08
19	0.02
20	0.005

TABLE I. Singular values for the first 21 Hermite-Gauss modes after optical clipping.

itation of the setup (it can be solved by the use of a larger cylindrical mirror), it did limit the maximum number of orthogonal modes that we could confidently measure in the experiment. That is the reason why we stop showing squeezing for mode orders larger than 21.

### Appendix F: Flat mode basis

The spectral flat mode basis discussed in the main text is constructed to be orthogonal, taking advantage of even and odd symmetries for the subsequent mode functions. It was specifically designed to roughly resemble the first 4 Hermite-Gauss modes, so that the spectral width of each flat mode was obtained by minimizing the  $l^2$  norm distance to the corresponding Hermite-Gauss mode counterpart. Fig. 10 shows the 4 flat modes constructed and implemented in the experiment, together with the first 4 Hermite-Gauss modes.

### Appendix G: Eigenmodes from the diagonalization of the covariance matrix

The numerical diagonalization of the covariance matrix performed in the main text gives back the eigenmode basis where there are no quantum correlations, sometimes called the supermode basis. For additional information concerning the reconstruction of the covariance matrix see [32].

We therefore expect the numerical eigenmodes to resemble discretized versions of the quasi-Hermite-Gauss

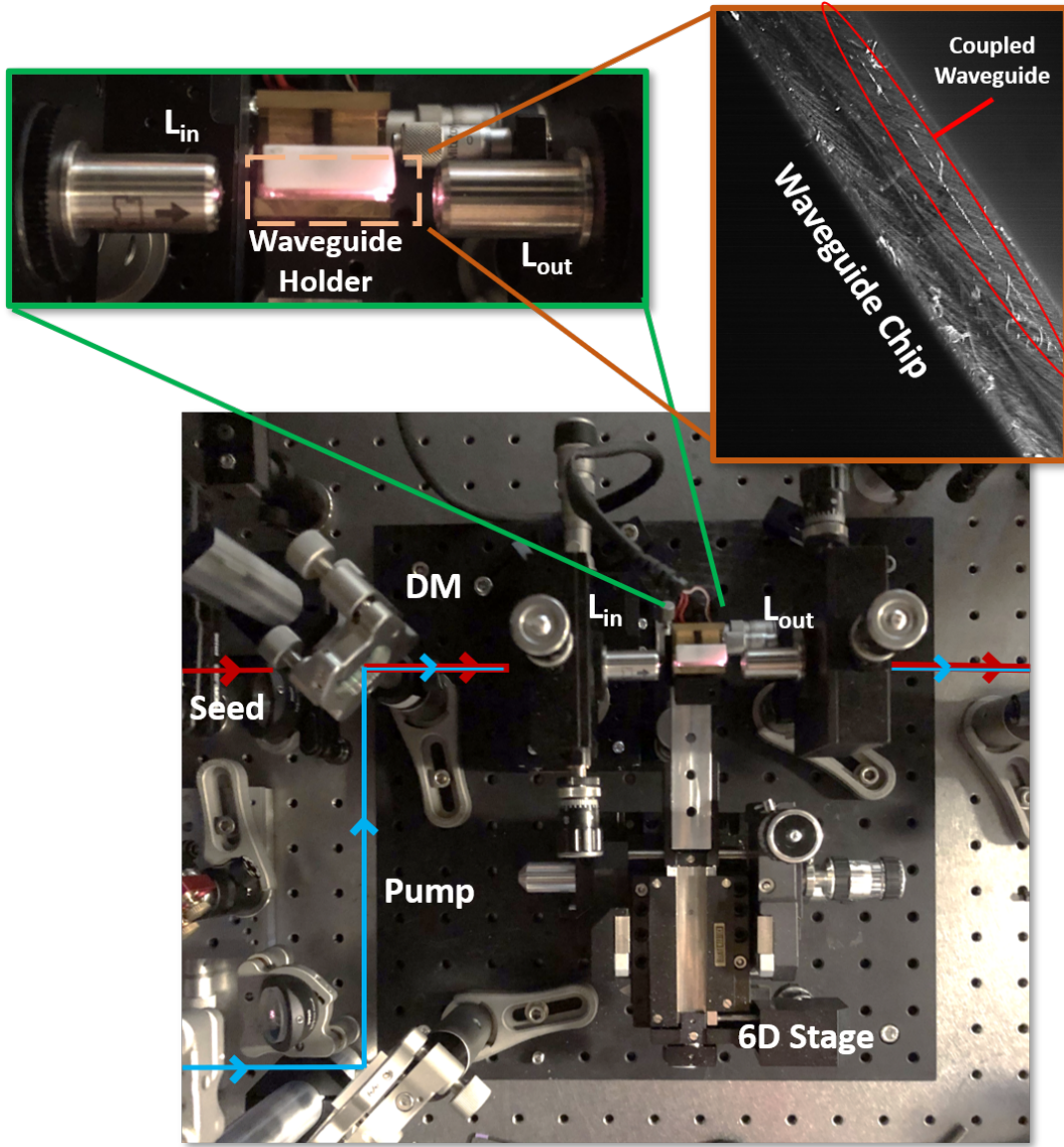


FIG. 8. **Waveguide characterization setup.** The seed (1560 nm) and the pump (780 nm) are coupled to the rectangular waveguide showed in the zoom at the upper right corner via the two lenses  $L_{in}$  and  $L_{out}$ . The waveguides are mounted on a 6D stage that allows sub-micrometric alignment for the waveguide couplings to both seed and pump fields. DM stands for Dichroic Mirror.

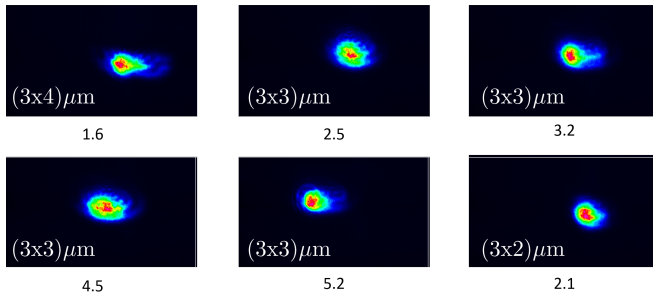


FIG. 9. **Spatial modes at 1560 nm.** Examples of the spatial modes measured after the waveguide coupling at telecom wavelengths for 6 different waveguides.

supermodes found in our numerical simulations.

Fig. 11 shows the numerical eigenmodes obtained after the diagonalization. In general, the supermode shapes are in very good agreement with the expected theoretical Hermite Gauss modes. The bandwidth of every Hermite-Gauss is systematically higher than the theoretical value and it's slightly higher than the total LO bandwidth for higher order modes, which can detriment the real value of squeezing present in the state compared to the presented measured values.

Note that the eigenvalues of the covariance matrix are directly related to the expected squeezing levels of each eigenmode. Fig. 12 shows the eigenvalues obtained in the diagonalization, which are consistent with those values

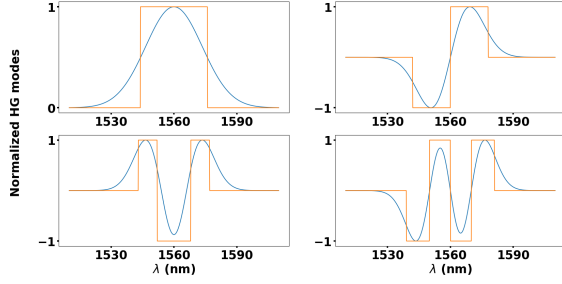


FIG. 10. First 4 Hermite-Gauss modes measured (blue) and the corresponding spectral flat modes obtained from them (orange).

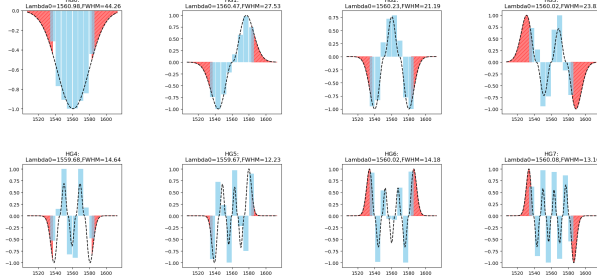


FIG. 11. Eigenmodes of the covariance matrix and a fit to HG modes. The wavelength outside of the Local Oscillator bandwidth due to optical clipping is depicted as the red areas.

directly measured in the HG basis from the main text.

### Appendix H: Cluster state measurement

As stated in the main text, we measured some few-nodes cluster states with different topologies corresponding to different adjacency matrices. The specific adjacency matrices used in this work are the following:

$$V_{\text{linear } 4} = \begin{pmatrix} 0 & 1 & 0 & 0 \\ 1 & 0 & 1 & 0 \\ 0 & 1 & 0 & 1 \\ 0 & 0 & 1 & 0 \end{pmatrix} \quad (\text{H1})$$

$$V_{\text{square}} = \begin{pmatrix} 0 & 1 & 0 & 1 \\ 1 & 0 & 1 & 0 \\ 0 & 1 & 0 & 1 \\ 1 & 0 & 1 & 0 \end{pmatrix} \quad (\text{H2})$$

$$V_{\text{star}} = \begin{pmatrix} 0 & 1 & 1 & 1 \\ 1 & 0 & 0 & 0 \\ 1 & 0 & 0 & 0 \\ 1 & 0 & 0 & 0 \end{pmatrix} \quad (\text{H3})$$

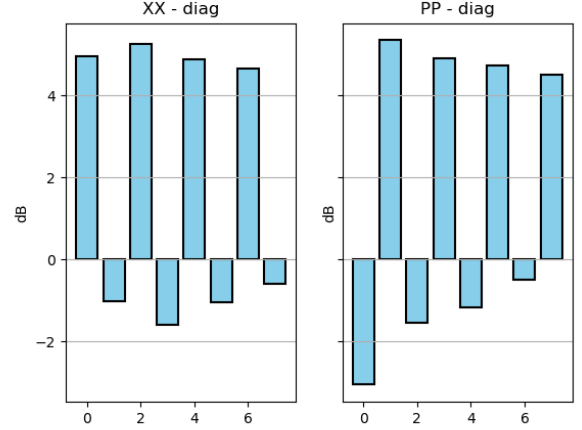


FIG. 12. Squeezing values obtained from the numerical diagonalization of the covariance matrix in the frequency basis. The modes have been arranged in decreasing order of anti-squeezed quadratures, and the first eigenmode is squeezed in the  $\hat{p}$  quadrature by convention.

$$V_{\text{linear } 6} = \begin{pmatrix} 0 & 1 & 0 & 0 & 0 & 0 \\ 1 & 0 & 1 & 0 & 0 & 0 \\ 0 & 1 & 0 & 1 & 0 & 0 \\ 0 & 0 & 1 & 0 & 1 & 0 \\ 0 & 0 & 0 & 1 & 0 & 1 \\ 0 & 0 & 0 & 0 & 1 & 0 \end{pmatrix} \quad (\text{H4})$$

$$V_{\text{linear } 8} = \begin{pmatrix} 0 & 1 & 0 & 0 & 0 & 0 & 0 & 0 \\ 1 & 0 & 1 & 0 & 0 & 0 & 0 & 0 \\ 0 & 1 & 0 & 1 & 0 & 0 & 0 & 0 \\ 0 & 0 & 1 & 0 & 1 & 0 & 0 & 0 \\ 0 & 0 & 0 & 1 & 0 & 1 & 0 & 0 \\ 0 & 0 & 0 & 0 & 1 & 0 & 1 & 0 \\ 0 & 0 & 0 & 0 & 0 & 1 & 0 & 1 \\ 0 & 0 & 0 & 0 & 0 & 0 & 1 & 0 \end{pmatrix} \quad (\text{H5})$$

We construct the nullifiers starting from the Hermite-Gauss basis used in the main text. The modes represented by the nodes of the cluster state are then a linear superposition of the Hermite-Gauss modes. The bandwidth of the nodes in the cluster is therefore the same as the presented HG bandwidth. The nullifiers are combination of quadrature operators of the node of the cluster, so that the measurement of their variance is done by setting as the LO mode a specific combination of the modes corresponding to the node of the clusters. We then measured the squeezing of each nullifier of a particular cluster state topology, i.e. a particular adjacency matrix, by averaging 15 squeezing traces, in the same manner as when measuring squeezing in the HG modes. The squeezing values of the nullifiers of a given cluster are expected to be very close, in particular they are expected to be the same for a perfect cluster. Therefore in the main text we

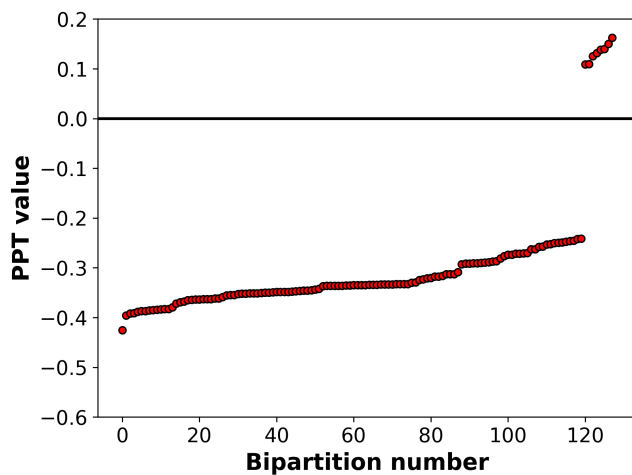


FIG. 13. PPT values computed for all 127 possible bipartitions. The results show that almost all (119) of the values are negative, thereby indicating the non-separability of the state.

use the statistical box plot representation for the mean squeezing value and its variance over all the nullifiers in the cluster.

As a technical note, we chose unweighted and undirected graphs in this text, thus assuming equal interac-

tion strength between all nodes for the generated clusters.

### Appendix I: Peres–Horodecki (PPT) criterion

The Positive Partial Transposition (PPT) criterion can be checked from the covariance matrix measurement to determine whether quantum correlations are present in our state in the frexel basis.

The PPT criterion is based on the fact that given a density matrix defining a quantum state, the partial transpose matrix of two possible bipartitions of the density matrix has to be positive defined for the two bipartitions being separable. The criterion applied to continuous variable systems can be found, for example, in [35]. This theorem applies to the covariance matrix since it completely defines any Gaussian state.

In our case, given that we have an 8x8 matrix in our frexel basis, we have a total of 127 possible bipartitions. For each bipartition, we can define the minimum eigenvalue of the partial transpose matrix as the PPT value, indicating quantum correlations if negative.

Fig. ?? shows the PPT value for the different bipartitions of our covariance matrix, showing the violation of the PPT criterion, *i.e.*, negativity in the partial transpose matrix, in 94% of them.

More details about the PPT criterion applied to the covariance matrix can be found in [41].